Manuscript Click here to view linked References

Internal Dynamics Interact with Proprioceptive Feedback During Movement Execution in a Model of Motor Cortex

Hongru Jiang[a,1], Xiangdong Bu[a,1], Zhiyan Zheng[a], Xiaochuan Pan[b,**] and Yao Chen[a,**]

[b]School of Mathematics, East China University of Science and Technology, Shanghai, 200237, China
[a]School of Biomedical Engineering, Shanghai Jiao Tong University, Shanghai, 200240, China

ABSTRACT

Neuronal population responses in motor cortex display low-dimensional rotational patterns, where neural state rotates consistently during movement execution. These patterns are thought to arise from the internal dynamics within motor cortex. However, external inputs such as proprioception also shape motor cortical activity. To investigate the roles of internal dynamics and proprioceptive feedback, we constructed an inhibitory stabilized network, with excitatory recurrence stabilized by inhibition, designed to control an arm model performing delayed reach task. The optimized network generated patterns similar to those observed in motor cortex data, demonstrating our model's plausibility. We designed a disruption strategy to dissect the contribution of internal dynamics and proprioceptive feedback, and found that disrupting internal dynamics significantly diminished rotational dynamics, whereas disrupting proprioceptive feedback led to ceaseless movement. Thus, internal dynamics dominate, while proprioceptive feedback fine-turns cortical pattern generation. Analysis of the ablation experiment revealed that proprioceptive feedback improved the robustness against noisy initial conditions by decreasing tangling in neural activity. Finally, our network still exhibited rotational dynamics when the arm moved at a constant speed, suggesting that these rotations could be prominent features of motor cortical activity.

1. Introduction

Movement, such as reaching, grasping, and speaking, is central to our interaction with the world. The motor cortex (MC), which orchestrates intricate neural pathways to generate motor command, is critical for planning and executing movement . Electrophysiological recordings in non-human primates have revealed that neural activity in the MC represents movement kinematics, including direction (Georgopoulos et al., 1982), velocity (Inoue et al., 2018) and isometric force (Sergio et al., 2005). However, this perspective only partially explains the complex and multiphasic neural responses(Kalaska, 2019).

With advances in recording technologies and computational methods, the focus on MC has shifted from the representation of output to how motor command is created (Figure 1A). Recent studies have emphasized that MC is a dynamical system: neural activity is captured by the dynamic rule, where the future state depends on its current state and input (Churchland et al., 2012, 2010; Shenoy et al., 2013; Vyas et al., 2020a). The neural population responses exhibited rotational dynamics, where neural populations rotate consistently in the same direction in their state space, revealing the nature of complex neural activity. The dynamical system perspective has paved the way for interpreting motor cortical activity via recurrent neural network (RNN) — a computational scaffold without manipulating on real brain. In one class of models, the MC is approximated as an autonomous dynamical system during movement execution, with negligible external input (Figure 1B) (Churchland et al., 2012; Hennequin et al., 2014; Sussillo et al., 2015; Zimnik and Churchland, 2021; Michaels et al., 2016). The neural activity evolves from the initial condition, defined as the neural state prior to movement onset (Afshar et al., 2011; Churchland et al., 2010), under the control of strong internal dynamics. These models not only generate neural responses similar to real data at single-cell level, but also display rotational dynamics at population level (Churchland et al., 2012). However, the autonomous dynamical system, sensitive to initial conditions, may not be reliable in real-world situations.

Alternatively, there is a growing recognition of the role that external inputs play in shaping motor cortical activity (Figure 1C). Situated within a vast and distributed brain network, the MC integrates various external inputs, such as sensory feedback (Sauerbrei et al., 2020; Kalidindi et al., 2021), thalamic (Sauerbrei et al., 2020; Logiaco et al., 2021) and cerebellar control (Kumar and Ma, 2023). Sensory feedback is critical in finely controlled movements, as the MC has to integrate multiple sensory information including proprioception, vision and tactile sensation, to generate precise commands. The dynamical system perspective is also reflected in the framework of optimal feedback control (OFC), wherein the MC acts as a feedback controller using the best estimate of sensory feedback to produce motor output (Lillicrap and Scott, 2013; Omrani et al., 2017; Todorov and Jordan, 2002). OFC, which has successfully explained experimental behavior (Scott, 2004; Todorov and Jordan, 2002), is also expected to shape motor cortical dynamics during movement execution (Herter et al., 2009; Perich et al., 2020). A recent study found that sensory feedback also exhibits rotational dynamics, suggesting that sensory feedback may be determinant in cortical pattern generation (Kalidindi

**Corresponding author
pxc@ecust.edu.cn (X. Pan); yao.chen@sjtu.edu.cn (Y. Chen)

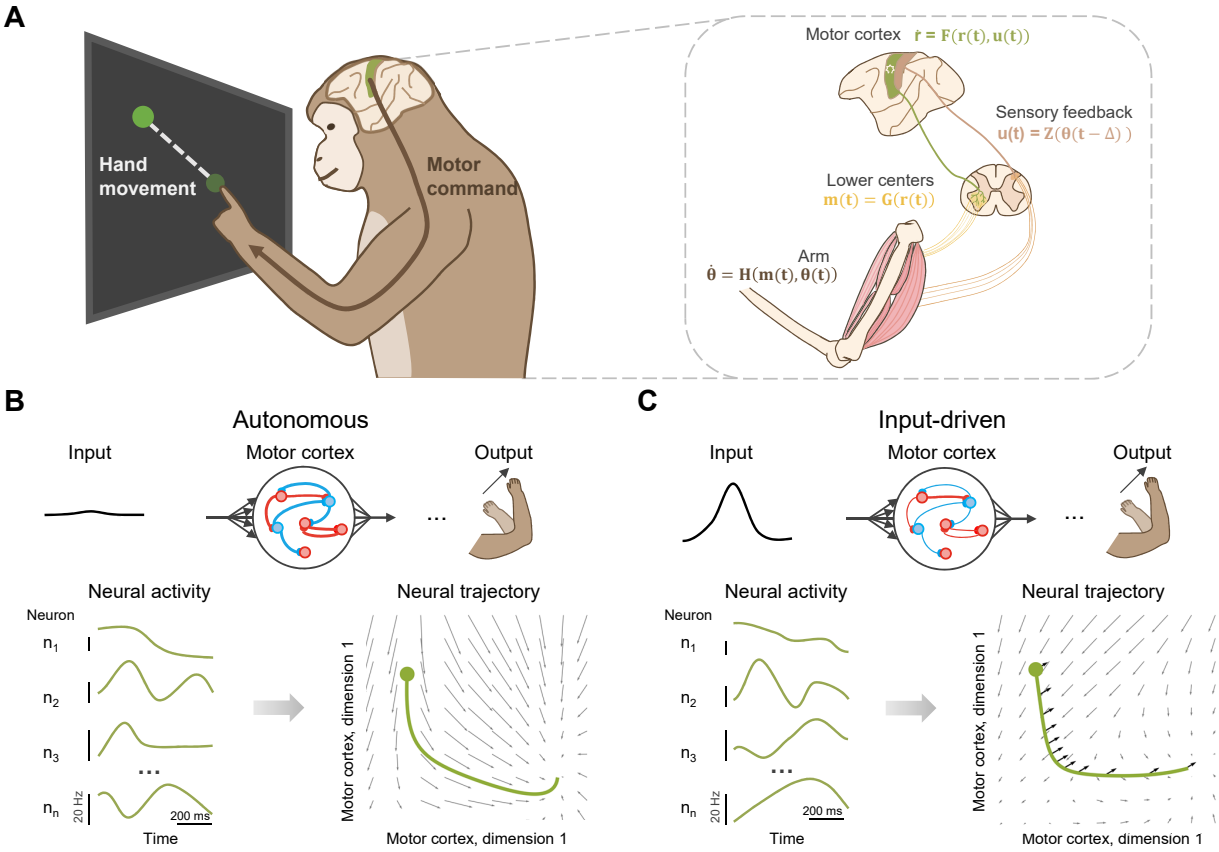

Figure 1: Motor cortex controls reaching under the perspective of dynamical system. (A) Dynamical system perspective on reaching movement. Left, illustration of the delayed reach task. A monkey sits in front of a screen, placing its hand on a central target to initiate the trial. A peripheral target then appears, signaling the location the monkey is to reach. After a randomized delay, a go cue (e.g., the central target disappears) prompts the monkey to reach the target. Right, dynamical system model of reaching. Motor cortical firing rates, evolving with a derivative $\dot{r}$, are determined by the internal dynamics in the MC and external input. Firing rates is converted into muscle activity $m(t)$ via a downstream circuit in lower motor centers, thereby updating the joint angles and velocities $\theta(t)$, ultimately reflected in hand movement. Delayed sensory feedback from the arm is sent back to the brain regions outside the MC. (B) MC as an autonomous dynamical system for movement execution. Neural activity is visualized in a low-dimensional state-space, with neural states evolving from specific initial conditions (solid circle) under strong internal dynamics within the MC (grey arrows). The length of arrows illustrates the strength of dynamics. (C) MC as an input-driven dynamical system for movement execution. Cortical activity starting from the initial condition, are driven by external input (black arrows) and internal dynamics (grey arrows). The internal dynamics are weaker than (C).

et al., 2021). Yet for the complete movement process, this model simplifies the external input as merely sensory information during preparatory period, potentially overstating the contribution of sensory feedback during movement execution.

Our study focuses on proprioceptive feedback, a critical component in motor control. The absence of proprioceptive feedback leads to significant motor deficits, even when visual feedback is available (Sainburg et al., 1995). We investigate the interaction between proprioceptive feedback and internal dynamics in the MC during movement execution. Utilizing an inhibitory stabilized network (Hennequin et al., 2014; Kao and Hennequin, 2019) that incorporated proprioceptive feedback from muscles and joints in an arm model, we simulated the delayed reach task. Our model generated firing rates that resembled real data at both single-cell and population levels, both qualitatively and quantitatively. Furthermore, we dissected the contribution of proprioceptive feedback and internal dynamics by disrupting them at graded percentage of timecourse. The internal dynamics disruption largely diminished rotational dynamics, whereas proprioceptive feedback led to ceaseless movement. These results suggest internal dynamics are pivotal in cortical pattern generation, while proprioceptive feedback is essential for speed control. Additionally, an ablation experiment revealed that proprioceptive feedback tames sensitivity to initial conditions by reducing tangling in neural activity, thus improves robustness. Finally, we integrated our model into a gated thalamo-cortical circuit model to perform tracking task, and observed rotational dynamics in the MC when the arm moved in constant speed, suggesting that rotations in neural activity are a prominent feature of the MC.

In summary, our research offers new insights into the intricate interaction between the MC's internal dynamics and proprioceptive feedback in movement generation, potentially reshaping our understanding of motor control.

2. Method

2.1. A model for movement generation

2.1.1. The MC network setup

We modeled the MC as an biologically plausible network, inhibition-stabilized network (ISN), satisfying Dale's law (neurons are either excitatory or inhibitory) (Hennequin et al., 2014; Eskikand et al., 2023). The ISN can produce rich and naturalistic neural responses, similar to real data. Our network comprised 150 excitatory and 50 inhibitory neurons (N=200 neurons) with a similar neuron proportion to that in the MC of non-human primates (Bakken et al., 2021; Chen et al., 2023).

Initially, we constructed a random connectivity matrix of size $N \times N$ with a connectivity density $p = 0.1$. The non-zero excitatory weights were drawn from a lognormal distribution with mean $log(w0)$ and variance 1, where $w_0^2 = r^2/(p(1-p))$ and r represents the initial spectral abscissa. For inhibitory weights, we employed a uniform distribution between -1 and 0. r is set to 1.2 for network receiving proprioceptive feedback, and 2.4 for the autonomous system network ensuring strong internal dynamics. Additionally, we initialized the network with global ("DC") population activity to fluctuate macroscopically, where DC mode is at -10 (Hennequin et al., 2012).

The random excitatory weights is stabilized by fine-tuned inhibitory architecture (Hennequin et al., 2014). We optimized the inhibitory synapses to minimize the "smoothed spectral abscissa" α_ϵ —the largest real part of among the eigenvalues of W, to below 0.3. The gradient of smoothed spectral abscissa with respect to the connectivity matrix W is expressed as

$$\frac{d\alpha_\epsilon(W)}{dW} = \frac{QP}{tr(QP)} \tag{1}$$

where Q and P are the observability and controllability Gramians of the system, respectively. These Gramians are defined as:

$$\begin{aligned} \mathrm{Q} &= \frac{2}{\tau}\int_0^\infty e^{(W^T-I)t/\tau}e^{(W-I)t/\tau}dt \\ \mathrm{P} &= 2\int_0^\infty e^{t(W-I)}e^{t(W-I)^T}dt \end{aligned} \tag{2}$$

where I is the unit matrix. Q and P can be solved from Lyapunov equation.

2.1.2. Musculoskeletal Arm model

We constructed a two-link musculoskeletal arm model in the horizontal two-dimensional plane, driven by six lumped muscles (mono-articular shoulder flexors, mono-articular shoulder extensors, mono articular elbow flexors, mono-articular elbow extensors, biarticular flexors and biarticular extensors) (Lillicrap and Scott, 2013). First, muscle activity $m(t)$ was transformed into muscle force $f(t)$ via the force-length-velocity function:

$$f(t) = F_{lv}\left(a(t),\ m(t)\right) \tag{3}$$

where $a(t)$ is the current arm state, including angular positions $\theta = (\theta_1, \theta_2)$ and velocities $\dot{\theta} = (\dot{\theta}_1, \dot{\theta}_2)$ of the elbow and shoulder joints. F_{lv} is the force-length-velocity function described in (Lillicrap and Scott, 2013). The muscle force was subsequently mapped into joint torques $j(t)$:

$$\begin{aligned} j(t) &= \mathcal{M}f(t) \\ \mathcal{M} &= \begin{pmatrix} 2 & -2 & 0 & 0 & 1.5 & -2 \\ 0 & 0 & 2 & -2 & 2 & -1.5 \end{pmatrix} \end{aligned} \tag{4}$$

where $\mathcal{M}$ is an empirical moment arm matrix. The arm state evolved dynamically according to:

$$\ddot{\theta} = M(\theta)^{-1}\left(j(t) - X\left(\theta, \dot{\theta}\right) - \mathcal{B}\dot{\theta}\right) \tag{5}$$

where M is the inertia matrix, X is the centripetal and Coriolis forces, and $\mathcal{B}$ is the damping matrix representing joint friction. The above parameters are given by

$$M(\theta) = \begin{pmatrix} a_1 + 2a_2cos\theta_2 & a_3 + a_2cos\theta_2 \\ a_3 + a_2cos\theta_2 & a_3 \end{pmatrix} \tag{6}$$

$$X\left(\theta, \dot{\theta}\right) = a_2sin\theta_2\begin{pmatrix} -\dot{\theta}_2\left(2\dot{\theta}_1 + \dot{\theta}_2\right) \\ \dot{\theta}_1^2 \end{pmatrix} \tag{7}$$

$$\mathcal{B} = \begin{pmatrix} 0.05 & 0.025 \\ 0.025 & 0.05 \end{pmatrix} \tag{8}$$

where $a_1 = I_1 + I_2 + M_2L_1^2$, $a_2 = M_2L_1D_2$, and $a_3 = I_2$ in the Table 1. The position and speed of the hand are given by:

$$\begin{pmatrix} p_x \\ p_y \\ v_x \\ v_y \end{pmatrix} = \begin{pmatrix} L_1cos\theta_1 + L_2cos\left(\theta_1 + \theta_2\right) \\ L_2sin\theta_1 + L_2sin\left(\theta_1 + \theta_2\right) \\ \left(-\dot{\theta}_1\left(L_1sin\theta_1\right) + L_2\sin\left(\theta_1 + \theta_2\right)\right. \\ \left.-\dot{\theta}_2\left(L_2\sin\left(\theta_1 + \theta_2\right)\right)\right) \\ \left(\dot{\theta}_1\left(L_1cos\theta_1\right) + L_2\cos\left(\theta_1 + \theta_2\right)\right. \\ \left.-\dot{\theta}_2\left(L_2\cos\left(\theta_1 + \theta_2\right)\right)\right) \end{pmatrix} \tag{9}$$

2.1.3. Modeling framework for movement execution

To accurately model different neural activity involved in each phase, we divided the simulation into two phases: preparation before movement onset and execution thereafter. First, we designed an artificial model for movement execution (Figure 2). The neuronal activations are described by a vector $x(t) = \left(x_1, x_2, \ldots, x_N\right)^T$ evolves according to:

$$\tau\frac{dx}{dt} = -x(t) + Wr(t) + I_{sp}(t) + 10\left[BI_{pi}(t)\right]^+ \tag{10}$$

where τ is the single-neuron time constant, W is the synaptic weight matrix, $r(t) = max(0, x(t))$ are the corresponding

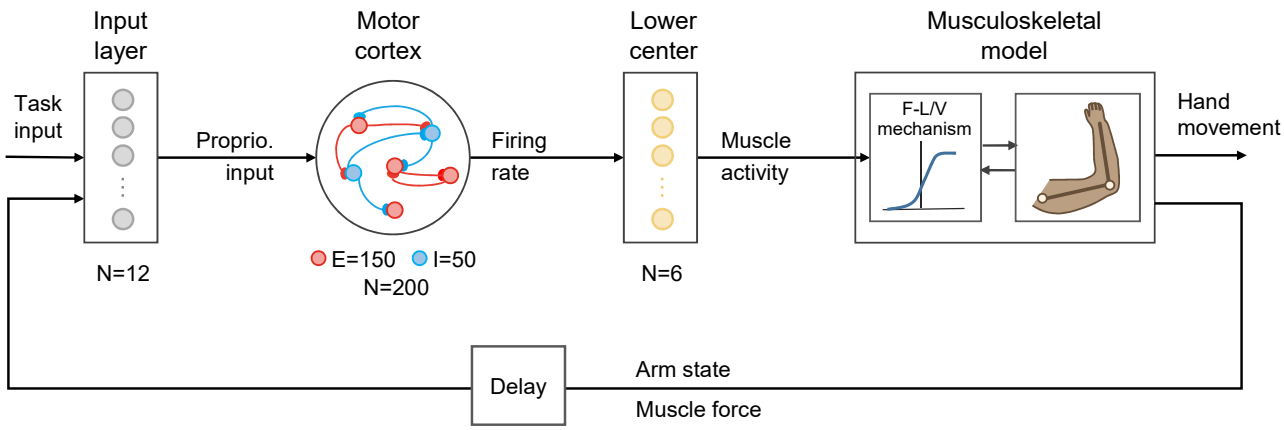

Figure 2: Schematics of our model for movement execution. The firing rates generated by MC network are translated into muscle activities via the lower center layer. Subsequently, the muscle activity is converted into muscle force through F-L/V mechanism and further into the arm state (angles and velocities of two joints) of two-link arm model, resulting in hand movements. Delayed proprioceptive feedbacks, including arm state and muscle forces, as well as task input, is transformed into proprioceptive input though the input layer.

Table 1
Parameters of the musculoskeletal arm model

Symbol	Description	Value	Unit
L_1	length of upper arm	0.30	m
L_2	length of lower arm	0.33	m
M_2	mass of lower arm	1	kg
D_2	center of mass of lower arm	16	cm
I_1	moment of inertia of upper arm	0.025	kg m^2
I_2	moment of inertia of lower arm	0.045	kg m^2

firing rates. $I_sp(t) = x_{sp} - Wr_{sp}$ maintains the spontaneous activity of the network throughout all the movement process, with x_sp is drawn i.i.d from $N(20, 9)$. B is the input weight matrix. The external input$I_pi(t)$ is composed of task-goal input (desired location of the arm) and delayed proprioceptive feedback. As proprioception includes the sense of body position and movement, as well as muscular effort, the feedback in our model encompasses delayed arm state $a(t-\Delta)$ and muscle force $f(t-\Delta)$. We set the feedback delay Δ to 50 ms, considering feedback takes at least 50 ms to reflect current goal (Pruszynski et al., 2014). $[]^+$ is the Tanh activation function. Experimental and computational results have proven that muscle activity can be reconstructed from a weighted sum of the MC firing rates (Kaufman et al., 2014; Russo et al., 2018; Sussillo et al., 2015). Thus, we defined the muscle activity as:

$$m(t) = [Cr(t)]^+ \tag{11}$$

where C is the readout weight matrix. The simulation of movement preparation is realized in a circuit model in next section.

2.1.4. Thalamocortical circuit model

We incorporate a thalamocortical circuit model (Kao et al., 2021) to elucidate the neural dynamics underlying movement preparation and execution. During movement preparation, basal ganglia disinhibited thalamic neurons, leaving them to interact with cortex. At the end of preparation, basal ganglia inhibited thalamic neurons then reopened the loop to trigger movement execution (Figure 3). To ensure both biological plausibility and computational feasibility, we implemented several constraints in our model: (1) the MC was divided into the MC and the MC layer 4, and all the connection in the circuit satisfied Dale law. (2) integration dynamics in the thalamus and the MC layer 4 is omitted. (3) muscle activity was artificially set to 0 during movement preparation, bypassing spinal cord modeling for posture control. The corresponding dynamics of our circuit model can be described as:

$$\begin{aligned} \tau\frac{dx}{dt} &= -x(t) + Wr(t) + u^* + K_{xz}\varphi(z(t)) \\ \frac{dz}{dt} &= -z + K_{zy}\varphi(y(t)) \\ \frac{dy}{dt} &= -y + K_{yx}\varphi(x(t)) \end{aligned} \tag{12}$$

where x, y, z are the neural activations of M1, M1-layer4 and thalamus, respectively. K_{xz} is the M1-L4 to M1 connectivity matrix of size $N \times L$, with $N \times L_E$ non-negative elements and $N \times L_I$ non-positive elements ($L_E = 100$ is the number of excitatory neurons and $L_I = 100$ is the number of inhibitory neurons in M1-L4, $L = L_E + L_I$). K_{zy} is the thalamus to M1-L4, connectivity matrix of size $L \times N_E$, with $L \times N_E$ non-negative elements. K_{yx} is the M1 to thalamus connectivity matrix of size $N_E \times N$, with $N_E \times N$ non-negative elements. Note, $K = K_{xz}K_{zy}K_{yx}$ summarizes these three connectivity matrices around the loop into one feedback gain matrix, which can be calculated from the method described

in (Kao et al., 2021). $u^* = x^* - (W + K)x^*$ is the tonic movement-specific input that given to the network during movement preparation and shut off after movement onset, driving cortical state into the initial condition of movement onset x^*.

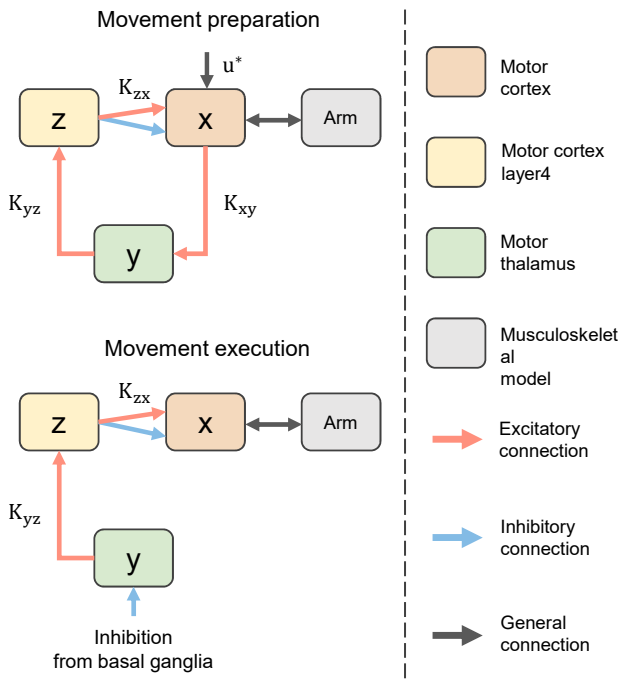

Figure 3: Schematics of thalamocortical circuit model for the whole movement process (see text).

2.1.5. Initial conditions at movement onset

The neural activity at movement onset significantly determines motor behavior (Pandarinath et al., 2018; Churchland et al., 2010). Here, we optimized movement-specific initial conditions, denoted as $\mathrm{x}^* = \left(\mathrm{x}_1^*, \mathrm{x}_2^*, \ldots, \mathrm{x}_7^*\right)$. These initial conditions are defined as a linear combination of the network's orthogonal input directions a and a weight matrix P.

$$\mathrm{x}_k^* = \sum_{i=1}^{200} P_{ki} a_i \tag{13}$$

This allows us to model diverse range of initial conditions associated with different conditions. In our model, various input directions evoke transient responses with varying amplitudes and durations. To quantified these responses, we introduced the concept of evoked energy $E(a)$ (Hennequin et al., 2014), defined as:

$$\mathrm{E(a)} = a^T Q a \tag{14}$$

where Q is the observability Gramian.

The full eigenvectors of Q, ordered by decreasing eigenvalues, define a collection $\left(a_1, a_2, \ldots, a_N\right)$ of N orthogonal input directions that each maximize the evoked energy. The corresponding eigenvalues are the evoked energies.

To tailor the initial conditions to specific tasks, we scaled the x^* so that $\|\mathrm{x}^*\|_2 = 9\sqrt{8N}$ in reach task, and $\|\mathrm{x}^*\|_2 = 4\sqrt{8N}$ in tracking task. Given that the network maintains spontaneous activity throughout all task phases, the true initial conditions are represented as $\mathrm{x}^* + x_{sp}$.

2.2. Network optimization

In the reach task, our goal was to optimize the model to reach the target a distance of $d = 10$ cm from the origin ($(0, 2d)$ from the shoulder). The speed profile of the reaching movement is defined as:

$$\mathrm{v(t)} = v_0 \left(\frac{t}{\tau_{\text{reach}}}\right)^2 \exp\left(-\left(\frac{t}{\tau_{\text{reach}}}\right)^2 /2\right) \tag{15}$$

where $\tau_{\text{reach}} = 0.14$ and v_0 is movement-specif to ensure hand reaches the target.

The recurrent architecture of the MC remains fixed after 2.1.1. We optimized movement-specific initial condition x_k^*, input weight matrix B and readout matrix C. To prevent movement from occurring at the end of preparation and spontaneously, we restrict the initial conditions x_k^* and spontaneous activity x_{sp} in the nullspace of C. The loss function was defined as:

$$\mathcal{L} = \frac{1}{8T} \sum_{k=1}^{8} \int_{\mathrm{t_{move}}}^{\mathrm{T}} \left\| v_k(t) - v_k^*(t) \right\|^2 dt + \alpha \mathrm{R}_{fc} + \beta \mathrm{R}_n + \mathrm{R}_b \tag{16}$$

where k is the number of movement condition and $\mathrm{T} = 900$ ms. The first term measures the squared error between the actual and desired hand velocities. The second term penalizes the muscle force after movement execution, defined as:

$$\mathrm{R}_{fc} = \frac{\alpha}{300} \sum_{k=1}^{8} \int_{\mathrm{T}-300}^{\mathrm{T}} \|f(t)\|^2 dt \tag{17}$$

where $\alpha = 0.1$ and $\mathrm{f(t)}$ is the muscle force.

The third term penalizes the distribution of neural firing rates, to prevent weak neural response in the first half of movement epcoh ($\beta = 1e^{-3}$), defined as:

$$\mathrm{R}_n = \frac{\beta}{300} \sum_{k=1}^{8} \max\left(0, \left(\int_{\mathrm{t_{move}}}^{\mathrm{t_{move}}+300} ||x(t) - x_{sp}||^2 dt - \int_{\mathrm{t_{move}}+300}^{\mathrm{t_{move}}+600} ||x(t) - x_{sp}||^2 dt\right)\right) \tag{18}$$

The last term penalizes the input weight difference between desired and actual arm location, defined as:

$$\mathrm{R}_b = \frac{1}{N} \left(\| \mathrm{B}_1 - \mathrm{B}_3 \|^2 + \| \mathrm{B}_2 - \mathrm{B}_4 \|^2 \right) \tag{19}$$

where B_1 and B_2 represent the weight of desired joint angles, B_3 and B_4 represent the weight of actual joint angles.

For the tracking task, we used gain modulation that controlled neuronal dynamics for flexible motor output (Stroud et al., 2018). As the dynamics of the MC remain approximately linear during movement execution, and equation 10 becomes:

$$\tau \frac{dx}{dt} = -x(t) + gWx(t) + I_{sp}(t) + \left[BI_{pi}(t)\right]^{+} \quad (20)$$

where g is the gain modulation factor. We optimized g, initial condition x_k^*, input weight matrix B, and kept the readout matrix C fixed. The loss function was defined as:

$$\mathcal{L} = \frac{1}{8T}\sum_{k=1}^{8}\left(\int_{L_{\text{mave}}}^{\text{T}} \left\|p_k(t) - p_k^*(t)\right\|^2 dt + \alpha \int_{L_{\max}}^{\text{T}} \left\|v_k(t) - v_k^*(t)\right\|^2 dt\right) + \beta \text{R}_n + \text{R}_b \quad (21)$$

where p_k is the hand position and p_k^* is the target position. $\alpha = 1e^{-2}$, $\beta = 1e^{-4}$.

2.3. Statistical analysis

2.3.1. jPCA Analysis

jPCA is a dynamical variant of principal component analysis(PCA) that extracts the rotational dynamics within neural population in a low-dimensional space (Churchland et al., 2012). We first used PCA to reduce the dimensionality of data $X \in R^{\text{n}\times ct}$ to $X_{red} \in R^{\text{k}\times ct}$, where n is the number of neurons, c is the number of reach conditions, and t is the number of time points, k is the number of principal components (PCs). jPCA considers the neural activity can be fitted into a linear dynamical system $\dot{X}_{\text{red}} = MX_{\text{red}}$, where M is the state-transition matrix. We found the unconstrained M that best fits the data X, and also identified a constrained skew-symmetric matrix M_{skew} that has purely imaginary eigenvalues, in the form of $X_{\text{red}} = M_{skew}X_{\text{red}}$. The two leading eigenvectors of the M_{skew} define the plane where the neural trajectory rotates most strongly.

Firing rates in our model include 8 conditions, 200 neurons, and a 600 ms duration after movement onset. Comparatively, Monkey N's data comprises 8 conditions, 202 neurons, and a 600 ms duration, starting 50 ms before movement onset. Firing rates were projected onto six PCs, while muscle activity and arm state were projected onto four PCs. For the reach task, we analyzed a 300 ms period after movement onset, and for the tracking task, a 750 ms period post-movement onset.

2.3.2. Canonical-correlation analysis

Canonical-correlation analysis (CCA) was to identify the common patterns in firing rates between model and real data. We focused on a 500 ms period after movement onset for comparison. Dimensionality reduction via PCA was first applied to both datasets: model data was projected onto 14 PCs, and monkey data onto 20 PCs. This reduction captured 95% of the variance in each dataset, ensuring correlations were not driven by low-variance data. Subsequently, we computed canonical variables and their correlations within these dimensionally-reduced datasets.

2.3.3. Tangling of neural trajectories

The MC is characterized by a low tangling of neural trajectories, indicative of similar neural states having dissimilar derivatives (Russo et al., 2018). The tangling of neural trajectories is quantified as:

$$Q(t) = \max_{t'} \frac{\left\|\dot{\boldsymbol{x}}_t - \dot{\boldsymbol{x}}_{t'}\right\|^2}{\left\|\boldsymbol{x}_t - \boldsymbol{x}_{t'}\right\|^2 + \varepsilon} \quad (22)$$

where $\boldsymbol{x}_t$ is the neural state at time t, $\dot{\boldsymbol{x}}_t$ is the temporal derivative of the neural state, $\|\cdot\|$ is the Euclidean norm, and ε is a small constant to prevent division by zero. If there is a state that is similar at different times but has similar corresponding derivatives, $Q(t)$ will be very large, suggesting high tangling. In our analysis, the neural state $x_t \in R^{\text{k}\times c\times t}$ was obtained by PCA, where k = 8. We computed $Q(t)$ across different movement conditions and at
different times within the same condition, using the methods described in Russo et al. (2018).

2.3.4. Population ratio

As illustrated in Figure 7B,C, the population ratio is defined as:

$$\|x_{dis}(t) - x_{sp}\| / \|x_{ctr}(t) - x_{sp}\| \quad (23)$$

where $x_{dis}(t)$ is the neural activity in disruption trial, $x_{ctr}(t)$ is the neural activity in control trial. We first removed the spontaneous activity and computed the magnitude of the population activity, which is the vector norm across all neurons. We then compared this magnitude to that in control trial, and averaged the ratio across all conditions. The population ratio quantifies the changes of population activity after different disruptions.

3. Results

3.1. Neural patterns in the motor cortex network

Our optimized ISN model effectively simulated straight reaching movements with desired velocity profiles, and muscle activations diversely changed the joint angles of shoulder (Figure 4A). The firing rates of individual neurons separated across movement conditions were similar to those observed in monkey the MC data (Figure 4B).

Further analysis using jPCA (fitting to a constrained linear dynamical system) revealed rotational dynamics in the firing rates of model, similar to those in the real data (Figure 4C). The rotational frequencies were 1.93, 1.18, 0.07 Hz for the model, and 1.66, 1.03, and 0.03 Hz for the monkey data. The total variance captured by the three jPC planes was 87% for the model and 79% for the monkey data. To further compare the firing rates of model and monkey quantitatively, we performed canonical-correlation analysis (CCA), which finds the common patterns between two datasets. We found patterns of model and monkey matched strongly among the canonical variables (Figure SS1A, B). The above resemblances validated the model's capability in capturing the prominent features of MC. Moreover, muscle

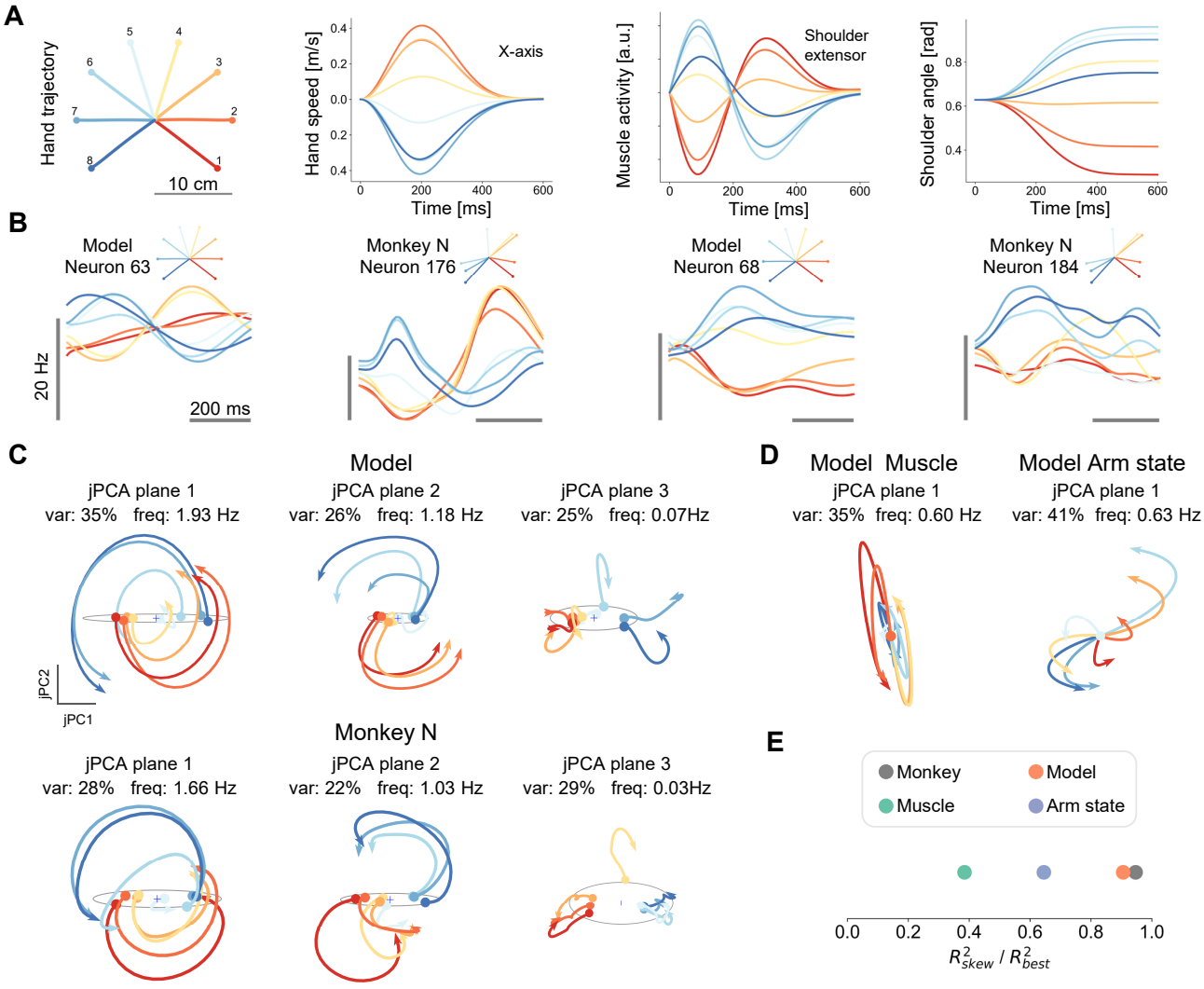

Figure 4: Motor cortex controls reaching under the perspective of dynamical system. (A) Reaches produced by the arm model, as well as x-y velocities of the hand, six muscles' activity, angles of shoulder and elbow joints for the movement condition traced in blue. Scale bar: 10 cm. (B) Firing rates of representative neurons in the model and monkey. Traces are colored according to the hand trajectories. Vertical bar: 20Hz. Horizontal bar: 200 ms. (C) Firing rates of model (left) and monkey (right) were projected into top three jPC planes. Each trace for one condition represents the evolution of the neural activity over 300 ms from the initial condition (circle); Traces are colored according to the preparatory state projection onto jPC_1. Grey ellipse shows the range of initial conditions. (D) Muscle activity and arm state from model were projected into top jPC plane. (E) The ratio between the fitting qualities for the constrained and unconstrained dynamical systems. Firing rate, muscle activity and arm state from model, along with firing rate from monkey data were assessed.

activity did not show consistent rotations, whereas the arm state display obvious rotational pattern (Figure 4D). Our simulation obtained similar result as the previous studies (Churchland et al., 2012; Kalidindi et al., 2021).

We also fit firing rates to an unconstrained linear dynamical system which provided the best fit. When comparing the goodness of fit R^2 for constrained and unconstrained dynamical systems, both monkey data and model achieved good fitting qualities. However, the arm state and muscle activity shew varying degrees of fitting quality (Figure 4E). This result implies that rotational dynamics are prominent in neural firing rates, but not directly correspond to muscle activity or arm state.

In summary, our ISN model has successfully replicated key features of MC activity in reach task, setting the stage for further investigations into the cortical pattern generation.

3.2. Internal dynamics dominates in cortical pattern generation

To investigate the contribution of internal dynamics and proprioceptive feedback in the MC to movement generation, we introduced a strategy that disrupted internal dynamics or proprioceptive feedback 25%, 33%, 50%, 100% timecourse during reaching (Figure 5A); that is, only internal dynamics

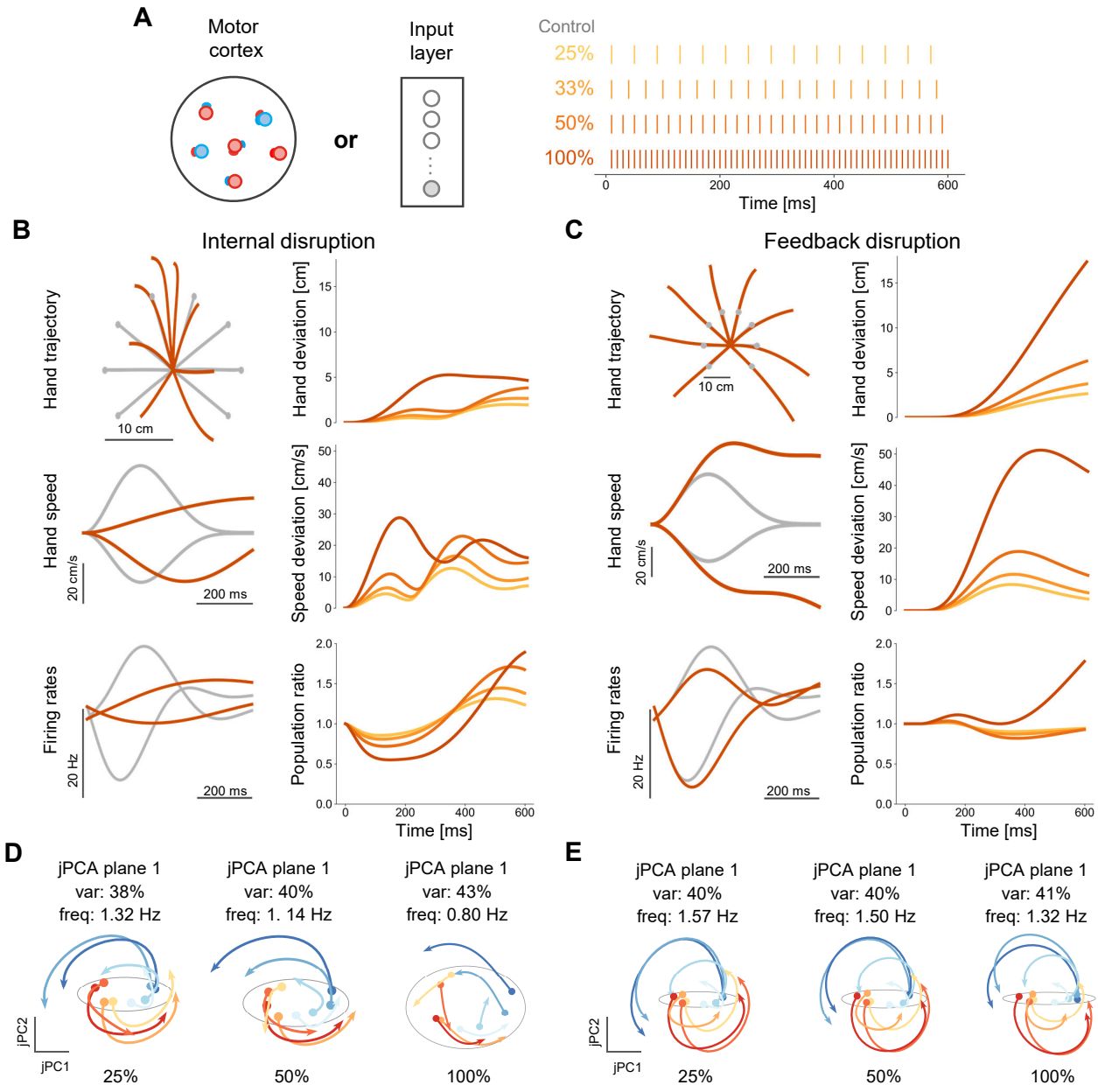

Figure 5: The contribution of proprioceptive feedback and the MC internal dynamics. (A) Illustration of graded disruption. The weights of internal recurrent connections or proprioceptive inputs was set to zero from 25% to 100% timecourse respectively. Note, the task input was not corrupted. (B) The influence of internal dynamics disruption on hand movement and neural activity. Top, hand trajectory after disruption compared to the control trial (only 100% was shown for clarity), and condition-averaged Euclidean distance from the hand position to the control hand position at the same time point for different grades. Middle, x-y hand speed in condition 1 after disruption compared to the control trial, and condition-averaged Euclidean distance but for hand speed. Bottom, two neurons' firing rates in condition 1 after disruption compared to the control trial, and population ratio that quantifies the firing rate fluctuation relative to that in control trial. (C) Same as (C) except for proprioceptive feedback disruption. (D) Firing rate after the graded disruption of internal dynamics projected into the top jPC plane. (E) Same as (D) except for the graded disruption of proprioceptive feedback.

(proprioceptive feedback) contribute to movement generation when proprioceptive feedback (internal dynamics) is disrupted.

Internal dynamics disruption led to obvious deviation from the original hand trajectory and suppressed firing rate fluctuations (Figure 5B), suggesting internal dynamics is critical in guiding the goal and transient behavior of neural activity in the MC. In contrast, proprioceptive feedback disruption resulted in ceaseless hand movement towards the target, suggesting proprioceptive feedback may be critical in terminating movement. We detected changes in hand velocity at 100 ms after movement onset, and changes in firing

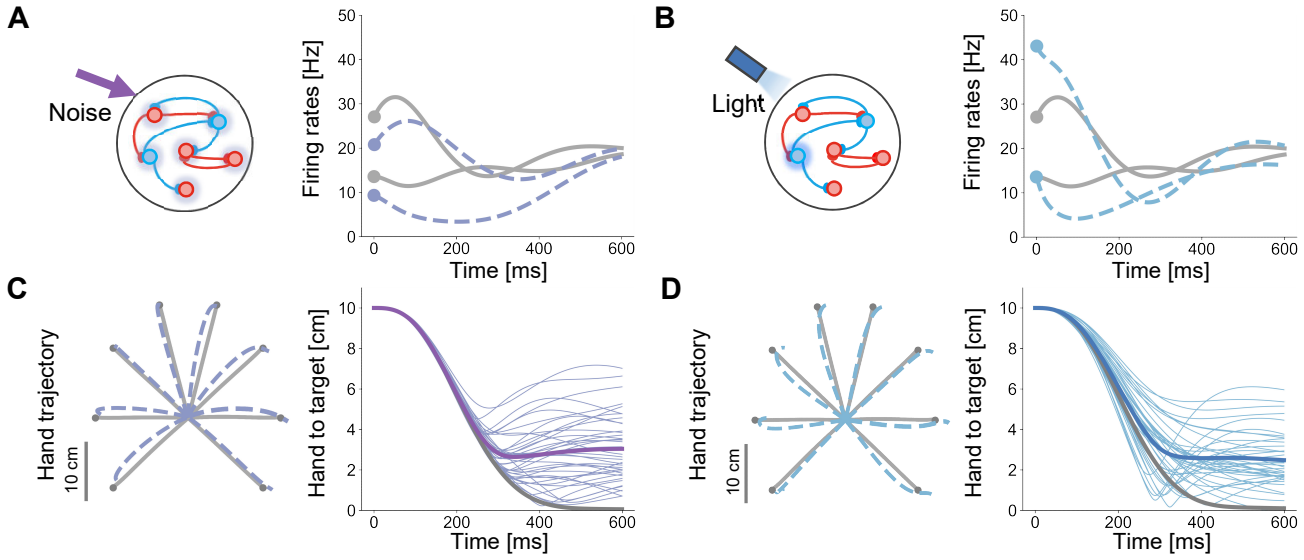

Figure 6: Proprioceptive feedback improves the robustness. (A) Illustration of noise perturbation. Left, white Gaussian noise was provided to every neuron in the network. Right, neural activity (purple dashed line) evolved after initial perturbation compared to the control trial trial (solid grey lines). Two example neurons are shown. (B) Illustration of optogenetic perturbation. Left, 30% of inhibitory neurons were activated by positive input. Right, neural activity (blue dashed line) evolved after initial perturbation compared to the control trial trial. (C) Hand movement after perturbed perturbation. Left, Hand trajectories in the presence (purple dashed) and absence (gray solid) of noise in the initial condition for one trial. Right, the distance of the hand to the target position over time. The thick purple lines denote the average distance of 40 trials (thin purple lines), and the grey line denoted the control trial. (D) Same as (C) except for optogenetic perturbation (shown in blue).

rates preceded velocity by 40 ms. Proprioceptive feedback disruption had a moderate effect on firing rate fluctuations (Figure 5C), indicating that proprioceptive feedback may be more involved in fine-tuning motor commands rather than generating them. Furthermore, the results of jPCA revealed the more pronounced impact of internal dynamics disruption on rotational dynamics, compared to proprioceptive feedback disruption (Figure 5D, E). The rotational dynamics were significantly diminished when internal recurrent architecture was removed, highlighting the dominant role of internal dynamics in generating these neural patterns.

In summary, our result show that internal dynamics play a dominant role in generating neural patterns, whereas proprioceptive feedback is integral to the fine-tuning of motor output.

3.3. Proprioceptive feedback tames sensitivity to initial conditions

Initial conditions should tolerate the large neural variability; for example, different initial conditions could result in similar movements (Churchland et al., 2006, 2010). Here, we manipulated the initial conditions into an aberrant state via two strategies in 40 trials. First, we added white Gaussian noise with SNR 20 dB to the initial conditions (Figure 6A), observing that our model executed movement with acceptable deviation (Figure 6C). Second, we employed a photoinhibition strategy that silenced the neural activity by providing strong excitatory input to a random subset of inhibitory neurons at movement onset (Figure 6B). Our model also behaved robustly (Figure 6D).

Moreover, we investigated the role of different types of proprioceptive feedback (joint angles, velocities, and muscle forces) in enhancing noise robustness. We designed an ablation experiment by building four submodels: a model without muscle force (sub-model 1), a model without angular velocity (sub-model 2), a model with only joint angles (sub-model 3), and an autonomous model (sub-model 4) (Figure 7A). Note, the autonomous network had strong internal dynamics that could transiently amplify initial conditions. After optimization, all the sub-models successfully completed the reach task and displayed rotational dynamics, however, they showed less resemblance to real data both qualitatively and quantitatively (Figure SS1C, D). The deviation from the target at the end of the movement increased, as the type of the proprioceptive feedback decreased (Figure 7B, C), indicating proprioceptive feedback improved the noise robustness of network. Importantly, network with proprioceptive feedback displayed "low tangling" in neural activity, which means moments where similar neural state led to dissimilar future state. We compared the tangling in sub-models $Q_subi, i = 1, 2, 3, 4$ with that in our model Q_model for every time across all the conditions (Figure 7D). After optogenetic perturbation, the tangling in our model is a slightly higher than that in sub-model 1, but lower than other sub-models. On the other hand, under Gaussian noise conditions, which caused larger movement deviations, our model exhibited consistently lower 'tangling' than sub-models.

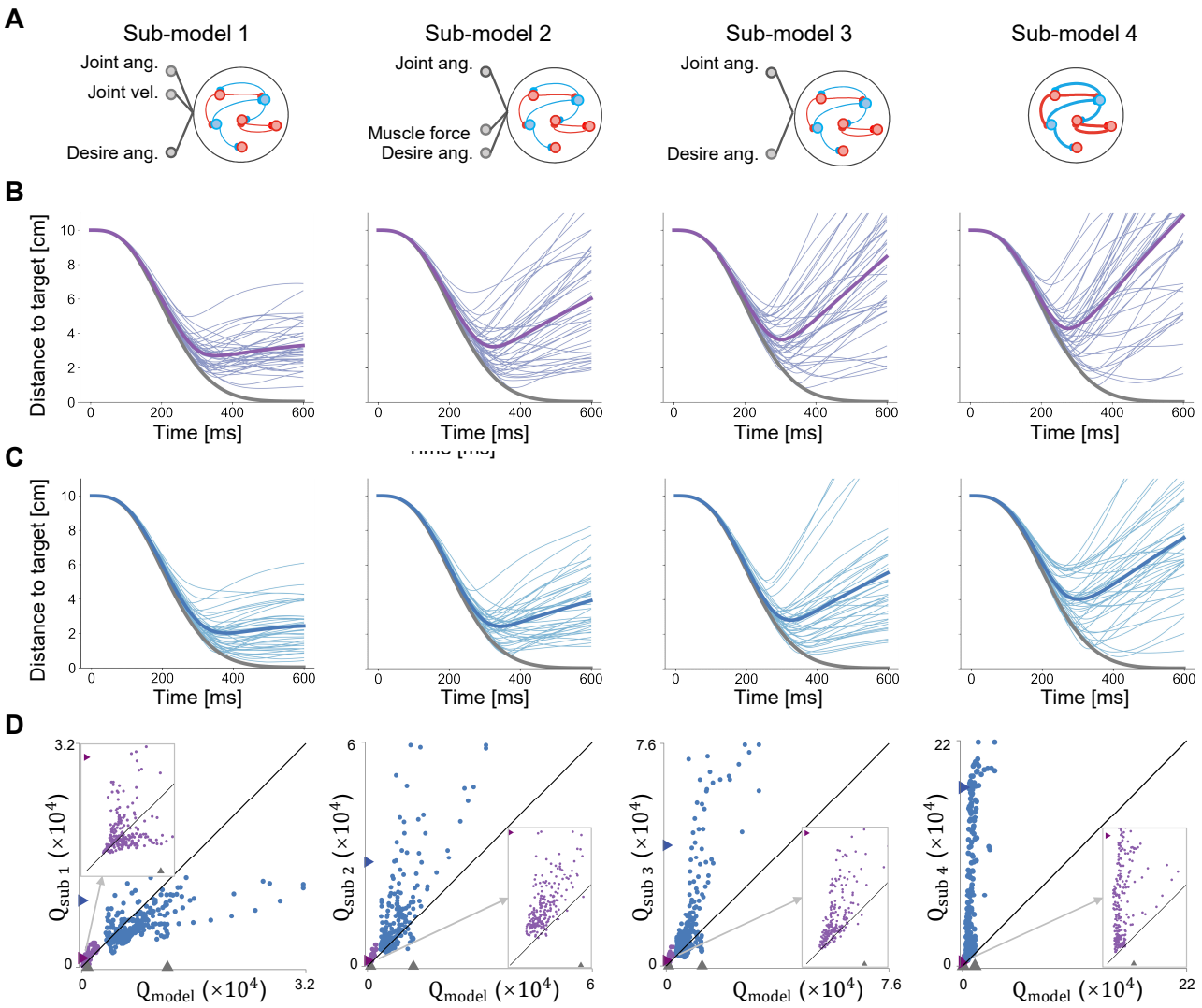

Figure 7: Sub-models executed reaching movement. (A) Ablation experiment of proprioceptive feedback. The bold lines in sub-model 4 indicate strong internal dynamics. (B) The distance of the hand to the target produced by sub-models after Gaussian noise perturbation (shown in purple) compared to the control trial (grey). (C) Same as (B) except for optogenetic perturbation (shown in blue). (D) Scatterplot of model versus sub-model tangling after two types of perturbations. Points are plotted for all times and conditions. The tangling after Gaussian noise perturbation is zoomed in for clarity. Black line indicates unity slope; triangles denote $90'h$ percentile tangling.

In conclusion, proprioceptive feedback is essential in motor cortical pattern generation. It tames the sensitivity to initial conditions by decreasing the tangling of the network.

3.4. Thalamocortical Circuit model for reaching and tracking

We tended to the complete movement that encompasses preparation (between target-on and movement onset) and execution. We incorporated our model into a gated thalamocortical circuit model (Kao et al., 2021) (Figure 8A). Similar to a switching linear dynamical system (Linderman et al., 2017), the loop was gated ON at preparation onset and OFF at preparation offset under the control of basal ganglia. This loop, coupled with movement-specific input, drives the cortical state to an appropriate initial condition for movement generation. To initiate movement, the loop became opened and the movement-specific input was simultaneously withdrawn. The circuit model completed the reach task after 150 ms preparation (Figure 8A, top).

Furthermore, we explored the model's ability to perform a tracking task, where the hand tracks a constant velocity target. Note, the map between firing rates and muscle activity and recurrent architecture remained fixed in the simulation, we introduced gain modulation for sufficient flexibility (Stroud et al., 2018). Crucially, we designed a delayed initiation of hand movement (150 ms), allowing the MC waited for the target to travel a short distance before

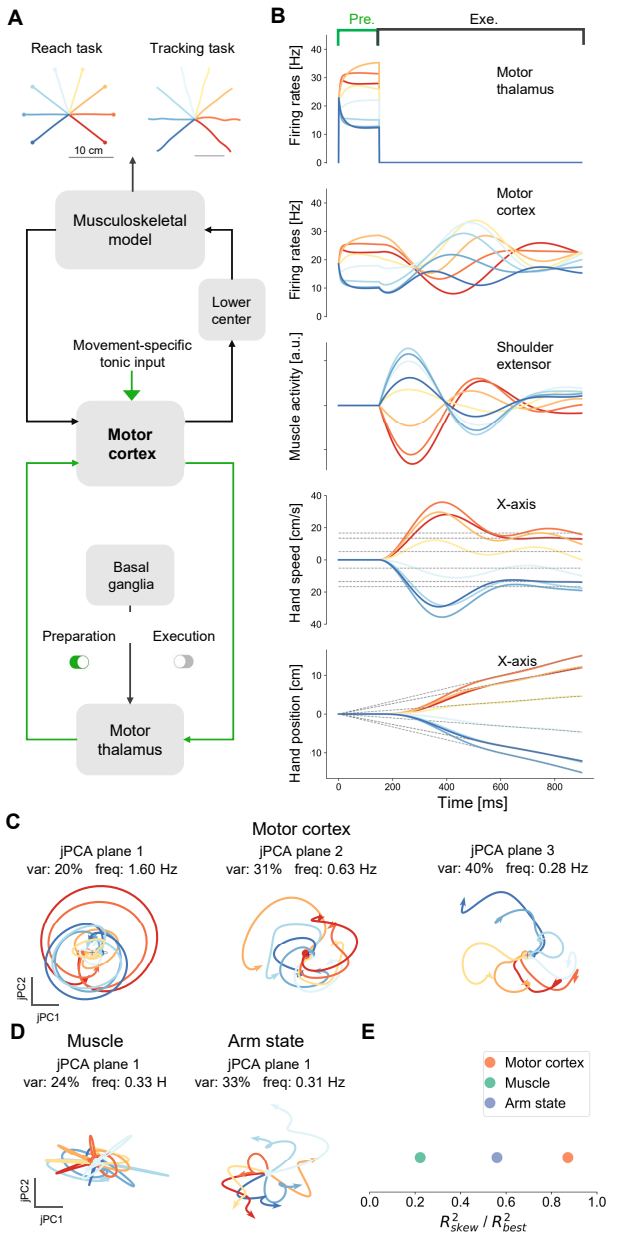

Figure 8: Movement preparation and execution via a gated cortico-thalamo-cortical loop. (A) Circuit model that executed reaching and tracking movement after 150 ms preparation. (B) Thalamic (top) and cortical activity (upper middle) generated muscle activity (middle) to track the target, shown in hand position (lower middle) and speed (bottom). Each trace represents one condition colored in (A). (C) Firing rates of motor cortex were projected into top three jPC planes. Each trace for one condition represents the evolution of the neural activity over 750 ms from the initial condition (circles); (D) Muscle activity and arm state from model were projected into top jPC plane. (E) The ratio between the fitting qualities for the constrained and unconstrained dynamical systems. The performance of firing rate, muscle activity and arm state were assessed.

triggering the movement. This delay is critical for preparing the initial condition for effective tracking movement.

After optimization, the thalamic activity driving the motor cortical activity from spontaneous state into an appropriate preparatory state, then initiated arm movement to catch and track the target (Figure 8A, B). The MC exhibited rotational dynamics on the first two jPC planes with total variance of 51%, however, the third jPC plane did not show rotation dynamics, capturing a large variance (Figure 8C). R^2 of constrained $\left(R^2_{\text{skew}}\right)$ and unconstrained $\left(R^2_{\text{best}}\right)$ dynamical systems were 0.68 and 0.78, which were decreased compared to the reach task. Besides, both the muscle activity $\left(R^2_{\text{skew}} = 0.02 \text{ and } R^2_{\text{best}} = 0.09\right)$ and the arm state $\left(R^2_{\text{skew}} = 0.14 \text{ and } R^2_{\text{best}} = 0.25\right)$ did not show rotational pattern (Figure 8D). A comparison of R^2_{skew} and R^2_{best} revealed that only the firing rate demonstrated similar fitting qualities in both constrained and unconstrained dynamical systems. In summary, the MC in our model still exhibited rotational dynamics when the arm moved at a constant speed.

4. Discussion

Motor cortical activity during movement epoch exhibits rotational dynamics unfolding from specific initial conditions (Churchland et al., 2012). However, it remains an open question whether these rotational dynamics are autonomously generated within the MC itself or are influenced by external inputs from other brain areas, as RNNs with or without external inputs (Hennequin et al., 2014; Kalidindi et al., 2021; Kao et al., 2021; Pandarinath et al., 2018; Suresh et al., 2020; Sussillo et al., 2015; Zimnik and Churchland, 2021) display rotational structure. In this study, we focus on the interaction between internal dynamics and proprioceptive feedback, both of which shape the motor cortical pattern and physical actions. We specifically investigated their roles in movement execution using an network model to perform motor task.

First, internal dynamics predominantly govern neural pattern generation during reaching. Disrupting internal dynamics greatly suppressed firing rates fluctuations and disrupted rotational dynamics. This may explain why many autonomous dynamical system models for the reach task achieve results similar to real data, as fast reaching movements are well pre-planned before initiation (Kao et al., 2021; Sussillo et al., 2015). Proprioceptive feedback plays a modulatory role in cortical pattern generation, but significantly influenced behavior. We observed that disrupting proprioceptive feedback led to continuous, unceasing movement towards the target. A study found that the temporal offset in visual feedback extended deceleration duration (McKenna et al., 2017); proprioceptive feedback in our model may have similar effect. Moreover, the incorporation of sensory feedback in brain-machine interfaces has been shown to enable more efficient robotic arm control (Flesher et al., 2021; Suminski et al., 2010).

However, our findings diverge from a previous study (Kalidindi et al., 2021) in which sensory feedback contributed substantially to cortical dynamics. This difference

may stem from the different methods of network analysis. First, we modeled the MC based on ISN, which was not trained for a particular movement, but contained a rich ensemble of quasi-oscillatory patterns that could be flexibly combined for the desired movement (Hennequin et al., 2014). This approach aligns with the dynamical systems perspective that the MC generates a set of basic patterns for a large repertoire of movements. Second, we optimized the initial conditions at movement onset rather than the recurrent connectivity of the network, as initial conditions significantly determine behavior (Pandarinath et al., 2018; Vyas et al., 2020a). Generally, research on how the MC generates reaching relies on a delayed-reach behavioral paradigm, where delay-period (ranged from 0 to 1000 ms) is artificially set to reflect the motor preparation and subjects must wait until a go cue onset before they could move (Churchland et al., 2006; Li and Cui, 2013; Li et al., 2018; Messier and Kalaska, 2000). Preparatory activity is critical for generating correct movements (Churchland et al., 2010; Vyas et al., 2020b). Kalidindi et al. (2021) used the sensory information as the external input during movement preparation. This simple feedforward strategy ignoring other input information could not capture the remarkable features of preparatory activity in reaching (Elsayed et al., 2016; Kaufman et al., 2014). Third, we employed a strategy of graded disruption (Sauerbrei et al., 2020) to dissect the contribution of proprioceptive feedback and internal dynamics. It could be rigid to infer from the amplitudes of currents generated from proprioceptive and internal dynamics source, since inputs positioned along the null-dimensions generate no output responses (Kao and Hennequin, 2019). Stavisky et al. (2017) showed that feedback-related motor cortical activity was isolated in null-dimensions that did not affect movement.

Second, proprioceptive feedback enhances the network's robustness. After perturbing the initial conditions with different strategies, the network with proprioceptive feedback still reached the target with only a small deviation, especially compared to the autonomous model, which was sensitive to small differences in initial conditions. Tolerance to the variably of initial conditions is critical in any biologically network, as motor noise is present in nervous system and different initial conditions can lead to qualitatively similar movements (Churchland et al., 2006). Proprioceptive feedback tames the sensitivity to initial conditions at movement onset. Moreover, the network with proprioceptive feedback displayed low tangling in neural activity, which was also observed in the MC across tasks and species (Russo et al., 2018). This low tangling contributes to noise robustness and ensures the reliable generation of motor commands.

Finally, rotational dynamics were a prominent feature of the MC in arm movement. We found that even when moving at a constant speed, the network still exhibited rotational pattern. On the other hand, Kalidindi et al. (2021) observed diminished rotational dynamics in the simulation of tracking task. This difference might stem from the omission of a preparatory period when training the network. We incorporated a brief preparatory phase into the network using a gated thalamocortical model, allowing neural activity to evolve from a prepared state rather than a spontaneous state. Rotational structure in the MC was widely observed during various movements, including reaching (Churchland et al., 2012), cycling (Russo et al., 2018), maintaining posture (Kalidindi et al., 2021), and speaking (Stavisky et al., 2019), but not in grasping (Suresh et al., 2020). Therefore, we could not exclude the possibility that rotational dynamics depend on the type of task. Neural recordings during the tracking task are essential to verify this assumption.

In conclusion, our model offers a computational framework to understand the interplay between cortical internal dynamics and proprioceptive feedback during movement execution. Nevertheless, there are some limitations in our model. First, our model omits the reaction period between the onset of the go cue and the onset of movement. During this period, sensory feedback has a limited effect, but internal dynamics and potential inputs, such as motor intention, are more likely to shape neural activity. Second, subjects use a flexible strategy that combines visual and proprioceptive feedback during reaching (Apker et al., 2011; Sober and Sabes, 2005), our model excluded visual feedback. Finally, future work will record experimental data of joint kinematics and cortical data from monkeys performing reach and tracking task in a horizontal two-dimensional plane.

References

Afshar, A., Santhanam, G., Byron, M.Y., Ryu, S.I., Sahani, M., Shenoy, K.V., 2011. Single-trial neural correlates of arm movement preparation. Neuron 71, 555–564.

Apker, G., Karimi, C., Buneo, C., 2011. Contributions of vision and proprioception to arm movement planning in the vertical plane. Neuroscience letters 503, 186–190.

Bakken, T.E., Jorstad, N.L., Hu, Q., Lake, B.B., Tian, W., Kalmbach, B.E., Crow, M., Hodge, R.D., Krienen, F.M., Sorensen, S.A., et al., 2021. Comparative cellular analysis of motor cortex in human, marmoset and mouse. Nature 598, 111–119.

Chen, A., Sun, Y., Lei, Y., Li, C., Liao, S., Meng, J., Bai, Y., Liu, Z., Liang, Z., Zhu, Z., et al., 2023. Single-cell spatial transcriptome reveals cell-type organization in the macaque cortex. Cell 186, 3726–3743.

Churchland, M.M., Byron, M.Y., Ryu, S.I., Santhanam, G., Shenoy, K.V., 2006. Neural variability in premotor cortex provides a signature of motor preparation. Journal of Neuroscience 26, 3697–3712.

Churchland, M.M., Cunningham, J.P., Kaufman, M.T., Foster, J.D., Nuyujukian, P., Ryu, S.I., Shenoy, K.V., 2012. Neural population dynamics during reaching. Nature 487, 51–56.

Churchland, M.M., Cunningham, J.P., Kaufman, M.T., Ryu, S.I., Shenoy, K.V., 2010. Cortical preparatory activity: representation of movement or first cog in a dynamical machine? Neuron 68, 387–400.

Elsayed, G.F., Lara, A.H., Kaufman, M.T., Churchland, M.M., Cunningham, J.P., 2016. Reorganization between preparatory and movement population responses in motor cortex. Nature communications 7, 13239.

Eskikand, P.Z., Soto-Breceda, A., Cook, M.J., Burkitt, A.N., Grayden, D.B., 2023. Inhibitory stabilized network behaviour in a balanced neural mass model of a cortical column. Neural Networks 166, 296–312.

Flesher, S.N., Downey, J.E., Weiss, J.M., Hughes, C.L., Herrera, A.J., Tyler-Kabara, E.C., Boninger, M.L., Collinger, J.L., Gaunt, R.A., 2021. A brain-computer interface that evokes tactile sensations improves robotic arm control. Science 372, 831–836.

Georgopoulos, A.P., Kalaska, J.F., Caminiti, R., Massey, J.T., 1982. On the relations between the direction of two-dimensional arm movements and cell discharge in primate motor cortex. Journal of Neuroscience 2, 1527–1537.

Hennequin, G., Vogels, T.P., Gerstner, W., 2012. Non-normal amplification in random balanced neuronal networks. Physical Review E 86, 011909.

Hennequin, G., Vogels, T.P., Gerstner, W., 2014. Optimal control of transient dynamics in balanced networks supports generation of complex movements. Neuron 82, 1394–1406.

Herter, T.M., Korbel, T., Scott, S.H., 2009. Comparison of neural responses in primary motor cortex to transient and continuous loads during posture. Journal of neurophysiology 101, 150–163.

Inoue, Y., Mao, H., Suway, S.B., Orellana, J., Schwartz, A.B., 2018. Decoding arm speed during reaching. Nature communications 9, 5243.

Kalaska, J.F., 2019. Emerging ideas and tools to study the emergent properties of the cortical neural circuits for voluntary motor control in non-human primates. F1000Research 8.

Kalidindi, H.T., Cross, K.P., Lillicrap, T.P., Omrani, M., Falotico, E., Sabes, P.N., Scott, S.H., 2021. Rotational dynamics in motor cortex are consistent with a feedback controller. Elife 10, e67256.

Kao, T.C., Hennequin, G., 2019. Neuroscience out of control: control-theoretic perspectives on neural circuit dynamics. Current opinion in neurobiology 58, 122–129.

Kao, T.C., Sadabadi, M.S., Hennequin, G., 2021. Optimal anticipatory control as a theory of motor preparation: A thalamo-cortical circuit model. Neuron 109, 1567–1581.

Kaufman, M.T., Churchland, M.M., Ryu, S.I., Shenoy, K.V., 2014. Cortical activity in the null space: permitting preparation without movement. Nature neuroscience 17, 440–448.

Kumar, G., Ma, C.H.E., 2023. Toward a cerebello-thalamo-cortical computational model of spinocerebellar ataxia. Neural Networks 162, 541–556.

Li, Y., Cui, H., 2013. Dorsal parietal area 5 encodes immediate reach in sequential arm movements. Journal of Neuroscience 33, 14455–14465.

Li, Y., Wang, Y., Cui, H., 2018. Eye-hand coordination during flexible manual interception of an abruptly appearing, moving target. Journal of neurophysiology 119, 221–234.

Lillicrap, T.P., Scott, S.H., 2013. Preference distributions of primary motor cortex neurons reflect control solutions optimized for limb biomechanics. Neuron 77, 168–179.

Linderman, S., Johnson, M., Miller, A., Adams, R., Blei, D., Paninski, L., 2017. Bayesian learning and inference in recurrent switching linear dynamical systems, in: Artificial Intelligence and Statistics, PMLR. pp. 914–922.

Logiaco, L., Abbott, L., Escola, S., 2021. Thalamic control of cortical dynamics in a model of flexible motor sequencing. Cell reports 35.

McKenna, E., Bray, L.C.J., Zhou, W., Joiner, W.M., 2017. The absence or temporal offset of visual feedback does not influence adaptation to novel movement dynamics. Journal of Neurophysiology 118, 2483–2498.

Messier, J., Kalaska, J.F., 2000. Covariation of primate dorsal premotor cell activity with direction and amplitude during a memorized-delay reaching task. Journal of neurophysiology 84, 152–165.

Michaels, J.A., Dann, B., Scherberger, H., 2016. Neural population dynamics during reaching are better explained by a dynamical system than representational tuning. PLoS computational biology 12, e1005175.

Omrani, M., Kaufman, M.T., Hatsopoulos, N.G., Cheney, P.D., 2017. Perspectives on classical controversies about the motor cortex. Journal of neurophysiology 118, 1828–1848.

Pandarinath, C., O'Shea, D.J., Collins, J., Jozefowicz, R., Stavisky, S.D., Kao, J.C., Trautmann, E.M., Kaufman, M.T., Ryu, S.I., Hochberg, L.R., et al., 2018. Inferring single-trial neural population dynamics using sequential auto-encoders. Nature methods 15, 805–815.

Perich, M., Conti, S., Badi, M., Bogaard, A., Barra, B., Wurth, S., Bloch, J., Courtine, G., Micera, S., Capogrosso, M., et al., 2020. Motor cortical dynamics are shaped by multiple distinct subspaces during naturalistic behavior (p. 2020.07. 30.228767).

Pruszynski, J.A., Omrani, M., Scott, S.H., 2014. Goal-dependent modulation of fast feedback responses in primary motor cortex. Journal of Neuroscience 34, 4608–4617.

Russo, A.A., Bittner, S.R., Perkins, S.M., Seely, J.S., London, B.M., Lara, A.H., Miri, A., Marshall, N.J., Kohn, A., Jessell, T.M., et al., 2018. Motor cortex embeds muscle-like commands in an untangled population response. Neuron 97, 953–966.

Sainburg, R.L., Ghilardi, M.F., Poizner, H., Ghez, C., 1995. Control of limb dynamics in normal subjects and patients without proprioception. Journal of neurophysiology 73, 820–835.

Sauerbrei, B.A., Guo, J.Z., Cohen, J.D., Mischiati, M., Guo, W., Kabra, M., Verma, N., Mensh, B., Branson, K., Hantman, A.W., 2020. Cortical pattern generation during dexterous movement is input-driven. Nature 577, 386–391.

Scott, S.H., 2004. Optimal feedback control and the neural basis of volitional motor control. Nature Reviews Neuroscience 5, 532–545.

Sergio, L.E., Hamel-Pâquet, C., Kalaska, J.F., 2005. Motor cortex neural correlates of output kinematics and kinetics during isometric-force and arm-reaching tasks. Journal of neurophysiology 94, 2353–2378.

Shenoy, K.V., Sahani, M., Churchland, M.M., 2013. Cortical control of arm movements: a dynamical systems perspective. Annual review of neuroscience 36, 337–359.

Sober, S.J., Sabes, P.N., 2005. Flexible strategies for sensory integration during motor planning. Nature neuroscience 8, 490–497.

Stavisky, S.D., Kao, J.C., Ryu, S.I., Shenoy, K.V., 2017. Motor cortical visuomotor feedback activity is initially isolated from downstream targets in output-null neural state space dimensions. Neuron 95, 195–208.

Stavisky, S.D., Willett, F.R., Wilson, G.H., Murphy, B.A., Rezaii, P., Avansino, D.T., Memberg, W.D., Miller, J.P., Kirsch, R.F., Hochberg, L.R., et al., 2019. Neural ensemble dynamics in dorsal motor cortex during speech in people with paralysis. Elife 8, e46015.

Stroud, J.P., Porter, M.A., Hennequin, G., Vogels, T.P., 2018. Motor primitives in space and time via targeted gain modulation in cortical networks. Nature neuroscience 21, 1774–1783.

Suminski, A.J., Tkach, D.C., Fagg, A.H., Hatsopoulos, N.G., 2010. Incorporating feedback from multiple sensory modalities enhances brain–machine interface control. Journal of Neuroscience 30, 16777–16787.

Suresh, A.K., Goodman, J.M., Okorokova, E.V., Kaufman, M., Hatsopoulos, N.G., Bensmaia, S.J., 2020. Neural population dynamics in motor cortex are different for reach and grasp. Elife 9, e58848.

Sussillo, D., Churchland, M.M., Kaufman, M.T., Shenoy, K.V., 2015. A neural network that finds a naturalistic solution for the production of muscle activity. Nature neuroscience 18, 1025–1033.

Todorov, E., Jordan, M.I., 2002. Optimal feedback control as a theory of motor coordination. Nature neuroscience 5, 1226–1235.

Vyas, S., Golub, M.D., Sussillo, D., Shenoy, K.V., 2020a. Computation through neural population dynamics. Annual review of neuroscience 43, 249–275.

Vyas, S., O'Shea, D.J., Ryu, S.I., Shenoy, K.V., 2020b. Causal role of motor preparation during error-driven learning. Neuron 106, 329–339.

Zimnik, A.J., Churchland, M.M., 2021. Independent generation of sequence elements by motor cortex. Nature neuroscience 24, 412–424.